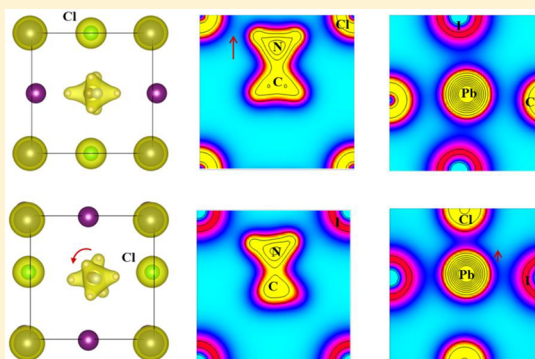


Effect of Chlorine Substitution on Lattice Distortion and Ferroelectricity of $\text{CH}_3\text{NH}_3\text{PbI}_3$

Wen-Li Yan,^{†,‡} Guang-Hong Lu,[†] and Feng Liu^{*,‡}[†]Department of Physics, Beihang University, Beijing 100191, P. R. China[‡]Department of Materials Science and Engineering, University of Utah, Salt Lake City, Utah 84102, United States

ABSTRACT: As a prototype of organic–inorganic hybrid perovskites, $\text{CH}_3\text{NH}_3\text{PbI}_3$ is attracting extensive attention because of its applications in high-power-conversion-efficiency solar cells. However, the mixed-halide perovskite $\text{CH}_3\text{NH}_3\text{PbI}_{3-x}\text{Cl}_x$ exhibited superior carrier diffusion properties in recent experiments. Using first-principles calculations and the Berry phase method, we calculated the crystal structures and ferroelectric properties of pure and Cl-doped $\text{CH}_3\text{NH}_3\text{PbI}_3$. The off-center displacement of Pb within the PbI_6 octahedron was found to introduce major intrinsic polarization, rather than the off-center displacement of CH_3NH_3^+ within the inorganic lattice or charge polarization within the organic cation, as expected. With chlorine substitution for iodine, the larger electronegativity difference between the halogen and Pb increases the lattice distortion and, hence, the electric polarization increases by as much as $\sim 50\%$, which provides a possible mechanism to further assist carrier separation and diffusion in solar cell devices.



Organic–inorganic hybrid perovskites has been attracting extensive attention since their debut in 2009 as light sensitizer in photovoltaic devices.¹ In comparison with their inorganic perovskite counterparts, the organic cation is expected to play multiple important roles in distorting crystal lattices and band structures, as well as creating local electrically polarized domains to help separate charge carriers. The materials exhibit the primary optoelectronic properties required in efficient photovoltaic devices, such as appropriate band gaps, high absorption coefficients, excellent carrier-transport properties, and apparent tolerance of defects,^{2,3} making them versatile as light sensitizers, light absorbers, and transport materials. The power conversion efficiencies (PCEs) of perovskite-based solar cells, mesostructured and planar, have experienced a rapid increase in the past several years and have reached 22.1% thus far.^{4–10}

Methylammonium lead iodide ($\text{CH}_3\text{NH}_3\text{PbI}_3$) is a prototype of the new hybrid perovskite, whose Pb and I ions compose corner-shared octahedra with a CH_3NH_3^+ cation occupying the center of each cuboctahedron surrounded by eight octahedra. At varying temperatures, $\text{CH}_3\text{NH}_3\text{PbI}_3$ has three different phases, orthorhombic ($Pnma$), tetragonal ($I4/mcm$), and cubic ($Pm3m$), in which the PbI_6 octahedra are tilted and rotated to different extents of symmetry.^{11–15} In the cubic phase (above $\sim 57^\circ\text{C}$),¹² the noncentrosymmetric CH_3NH_3^+ cation with C_{3v} symmetry must be orientationally disordered to satisfy O_h symmetry,¹¹ whereas in the tetragonal and orthorhombic phases, the cation orientation disorder is reduced.¹² The organic cation has an associated molecular dipole, a fundamental difference compared to the inorganic perovskite counterparts such as CsPbI_3 , in which the cation is spherically

symmetric. Band-structure calculations show the molecular energy levels to be far below or above the Fermi level,¹⁶ indicating that CH_3NH_3^+ has no direct impact on light absorption. However, there is other evidence that the organic cation has indirect influences on the band curvature^{17,18} and intrinsic ferroelectricity,¹⁹ by distorting the inorganic lattice. To explain the high performance of hybrid perovskite solar cells, Frost et al. proposed the “ferroelectric domain” mechanism according to which spontaneous electric polarization can assist the separation of photoexcited electron–hole pairs and reduce charge-carrier recombination.¹⁹ They also suggested ways in which the polarization can be tuned through a judicious choice of the organic cation.

When another halide anion (Cl or Br) was introduced into the iodide, the cell efficiencies based on the mixed-halide perovskites were further increased.^{6,8,20,21} Transient absorption and photoluminescence-quenching measurements determined the carrier diffusion length of $\text{CH}_3\text{NH}_3\text{PbI}_{3-x}\text{Cl}_x$ to be greater than $1\ \mu\text{m}$, 10 times longer than that of $\text{CH}_3\text{NH}_3\text{PbI}_3$.²² Aside from the improved transport properties, the band gap was measured to remain nearly identical to that of the triiodide,^{1,6} namely, $\sim 1.55\ \text{eV}$, which was also validated by first-principles calculations on $\text{CH}_3\text{NH}_3\text{PbI}_2\text{Cl}$.²³ Further investigations brought about some controversy regarding the miscibility of Cl in the parent $\text{CH}_3\text{NH}_3\text{PbI}_3$ lattice, and a Cl content on the order of 1% was inferred by comparison of the X-ray diffraction (XRD) patterns with $\text{CH}_3\text{NH}_3\text{PbI}_3$ samples and by X-ray

Received: June 20, 2016

Published: July 28, 2016

photoelectron spectroscopy (XPS) analysis.^{24–26} A limited Cl content in $\text{CH}_3\text{NH}_3\text{PbI}_{3-x}\text{Cl}_x$ can also be speculated on the basis of the calculated sizable destabilization energy of $\text{CH}_3\text{NH}_3\text{PbI}_2\text{Cl}$ (0.16 eV taking $\text{CH}_3\text{NH}_3\text{PbI}_3$ as a reference) because of the comparatively large difference in atomic radii between Cl and I.²³ However, under the assumption that Cl is actually present in the $\text{CH}_3\text{NH}_3\text{PbI}_3$ lattice, there could be local regions with comparatively large Cl content ratios, in which case the Cl atoms will impose sizable effect on the local structure and electric polarization. In light of the ferroelectric domain mechanism and the enhanced transport properties in $\text{CH}_3\text{NH}_3\text{PbI}_{3-x}\text{Cl}_x$, it is interesting to investigate the ferroelectricity enhancement upon Cl doping.

In this work, using first-principles calculations and the Berry phase method, we have calculated the crystal structures and ferroelectric properties of pure and Cl-doped $\text{CH}_3\text{NH}_3\text{PbI}_3$. The simplified calculation model of the high-temperature cubic phase and a large Cl content ratio was used here to qualitatively elucidate the effects of Cl doping. The ferroelectricity contributions from three sources were identified, namely, the off-center displacement of Pb within the PbI_6 octahedron, the off-center displacement of CH_3NH_3^+ within the inorganic lattice, and the charge polarization within the organic cation, with the first source identified as the major one. This work demonstrates that, upon Cl substitution for I, the larger electronegativity difference between the halogen and Pb increases the lattice distortion and, hence, the electric polarization increases by $\sim 50\%$, which provides a possible mechanism to further assist charge-carrier separation in solar cell devices.

As a reference, the structure and electric properties of an isolated CH_3NH_3^+ cation were first acquired using B3LYP/6-31(d) calculations in Gaussian 09.²⁷ The dipole moment was calculated to be 2.29 D, and the Mulliken population analysis indicated that 60.3% of the positive charge is located on the NH_3 group, consistent with recent literature reports.^{19,28} The electric dipole associated with the cation is oriented from C to N. The equilibrium cation structure was then incorporated into the perovskite cubic unit cell as an initial configuration for further density functional theory (DFT) bulk calculations using the Vienna Ab initio Simulation Package (VASP).²⁹

In the DFT calculations, the interactions between the electrons and ions were described using the projector augmented wave (PAW) method.^{30,31} We used the PBEsol exchange-correlation functional,³² which is intended to improve calculations of equilibrium properties such as bond lengths and lattice parameters compared to the previous scheme of Perdew, Burke, and Ernzerhof (PBE).³³ The potentials were obtained from the VASP package, using the valence electron configurations of $6s^25d^{10}6p^2$ for Pb, $5s^25p^5$ for I, $3s^23p^5$ for Cl, $2s^22p^3$ for N, $2s^22p^2$ for C, and $1s^1$ for H. The Brillouin zone was integrated using the tetrahedron method with Blöchl corrections.³⁴ A plane-wave kinetic energy cutoff of 500 eV was used to achieve good convergence. A Γ -centered Monkhorst–Pack³⁵ k -point grid of $8 \times 8 \times 8$ was used for the cubic unit cell, which converged the total energy to within 1 meV. Because we had little interest in this study in excited states or the exact band-edge structure, we did not use the relativistic GW calculations^{36,37} and did not take into consideration the spin–orbital coupling (SOC) for heavy atoms.^{38,39} Actually, SOC has been shown to have a very limited effect on atomic structure and ground-state properties.^{28,40}

For pure $\text{CH}_3\text{NH}_3\text{PbI}_3$, the cell volume was first determined by fitting a computed energy–volume curve to the Birch–Murnaghan equation of state,⁴¹ and then the atomic positions were optimized with an ionic force threshold of 0.01 eV/Å. The orientation of the CH_3NH_3^+ cation was found to have little influence on the total energy, and the rotation barrier of the organic cation was quite small, at ~ 30 meV. Therefore, we carried out calculations starting from three configurations with the axis of the organic cation oriented along the $\langle 001 \rangle$, $\langle 011 \rangle$, and $\langle 111 \rangle$ directions (as shown in Figure 1a) and chose from

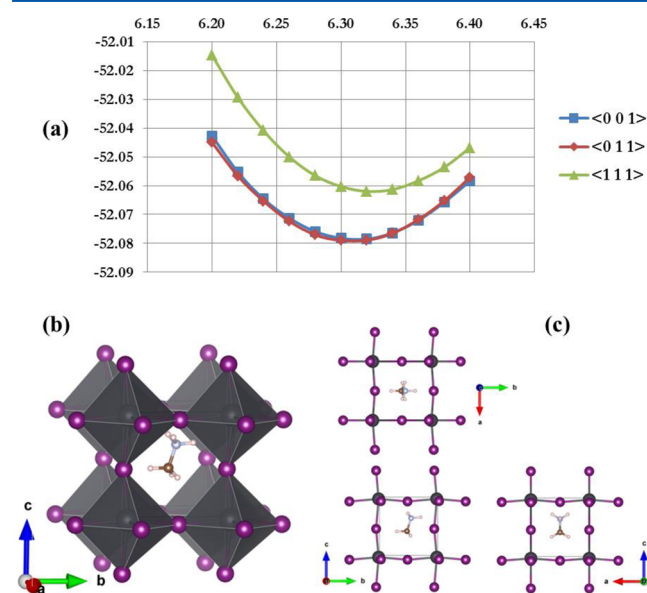


Figure 1. (a) Energy curve with varying lattice constants starting from three configurations with the axis of the organic cation oriented along the $\langle 001 \rangle$, $\langle 011 \rangle$, and $\langle 111 \rangle$ directions. (b) Equilibrium crystal structure of $\text{CH}_3\text{NH}_3\text{PbI}_3$ shown by the polyhedral model. (c) Views in the aob , boc , and coa planes shown by the ball-and-stick model. The structures in panels b and c were prepared using VESTA.⁴²

among the local minima the one with the lowest energy as the equilibrium structure of $\text{CH}_3\text{NH}_3\text{PbI}_3$. For Cl doping, one iodine atom out of three in the cubic unit cell was substituted by Cl, with the cell volume and shape kept fixed to mimic the local environment, which was embedded and confined inside a large host crystal that was mostly unchanged.

The ferroelectric properties of the pure and mixed-halide perovskite were calculated by evaluating the Berry phase expressions for the macroscopic electronic polarization.^{43–45} Because of the periodic boundary condition (PBC) used in DFT calculations, the calculated polarization density along each axis is always different from the actual value by arbitrary integer or half-integer multiples of a constant, namely, polarization quanta.⁴⁶ The polarization quanta were evaluated as eR/V , in which e is the elementary charge, R is the length of lattice vector along the corresponding axis, and V is the volume of the cell. To identify the ambiguity of the polarization quanta, we conducted a series of static calculations evolving from a constructed antiferroelectric (AFE) phase to the equilibrium ferroelectric (FE) phase and derived a smooth curve by adjusting the multiplicities of polarization quanta.

■ PURE IODIDE

The calculated equilibrium structure of the $\text{CH}_3\text{NH}_3\text{PbI}_3$ cubic phase is shown in Figure 1b, and the lattice constant is 6.31 Å,

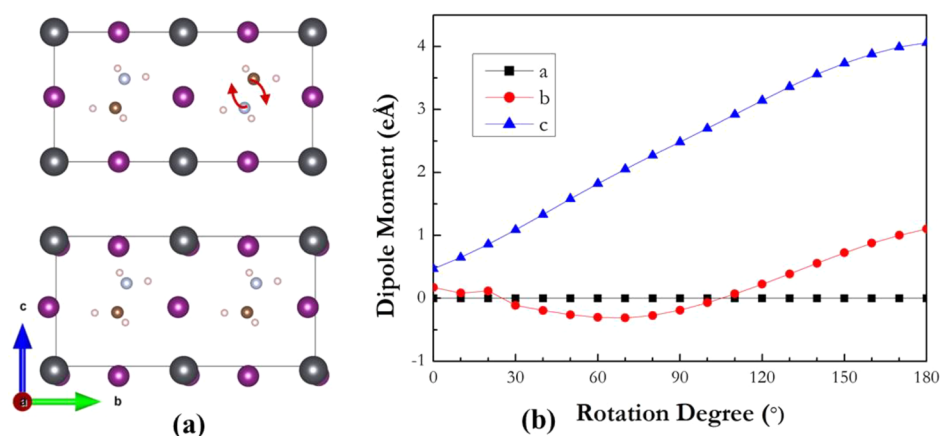
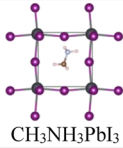
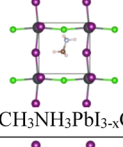
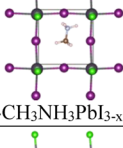
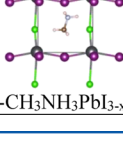


Figure 2. (a) Constructed AFE configuration (top) and the FE supercell (bottom). The arrows indicate the rotation of CH_3NH_3^+ along the AFE–FE evolving path. (b) Smooth curves of the dipole moments along the three axes for the $\text{CH}_3\text{NH}_3\text{PbI}_3$ supercell.

Table 1. Polarization Density of $\text{CH}_3\text{NH}_3\text{PbI}_{3-x}\text{Cl}_x$, Including Components along the Three Axes and Contributions from the Inorganic Lattice and the Organic Cation

Structure	Relative Energy (eV)	Polarization component			Polarization Magnitude ($\mu\text{C}/\text{cm}^2$)	
		notation	<i>a</i>	<i>b</i>		<i>c</i>
 $\text{CH}_3\text{NH}_3\text{PbI}_3$	--	all	0.00	3.51	12.96	13.42
		inorg.	0.00	1.24	5.61	5.74
		org.	0.00	1.43	4.47	4.70
 $\text{I-CH}_3\text{NH}_3\text{PbI}_{3-x}\text{Cl}_x$	0.11	all	0.01	2.27	10.83	11.07
		inorg.	0.01	0.09	3.39	3.40
		org.	0.00	1.37	5.27	5.45
 $\text{II-CH}_3\text{NH}_3\text{PbI}_{3-x}\text{Cl}_x$	0	all	9.76	4.71	9.34	14.31
		inorg.	9.85	2.22	1.63	10.23
		org.	0.33	1.15	5.25	5.39
 $\text{III-CH}_3\text{NH}_3\text{PbI}_{3-x}\text{Cl}_x$	0.08	all	0.00	1.68	21.43	21.49
		inorg.	0.00	0.58	13.48	13.49
		org.	0.00	1.44	4.49	4.72

in good agreement with the experimental value of 6.33 \AA .¹¹ The angle between the CH_3NH_3^+ cation axis and the $\langle 001 \rangle$ direction is 17.6° , and the C–N bond is contracted to 1.48 \AA because of the surrounding confinement, compared to 1.52 \AA in a vacuum. Because the NH_3 group is more positively charged than CH_3 (see the Mulliken population result from single-molecule calculations above), there are stronger hydrogen bonds between N and I ions, and the CH_3NH_3^+ cation is located significantly off-center within the inorganic lattice. Meanwhile, the Pb–I octahedra are severely distorted, with the Pb–I–Pb bond angle reduced to $\sim 170^\circ$ and Pb displaced vertically from the I–I diagonal by $\sim 0.25 \text{ \AA}$ (Figure 1c).

As a consequence of the polar CH_3NH_3^+ cations and the symmetry-breaking ionic displacements, ferroelectric polarization is induced.⁴⁷ The constructed AFE configuration and the equilibrium $1 \times 2 \times 1$ FE supercell are shown in Figure 2a,

in which the AFE configuration is constructed using a similar $1 \times 2 \times 1$ supercell, but with no distortion of the PbI_6 octahedron and with two organic cations directed in opposite directions. Accordingly, the Γ -centered Monkhorst–Pack k -point grid of $8 \times 4 \times 8$ was used for k -point sampling. The evolving configurations along the AFE–FE path were created by linearly interpolating Pb and I ions between AFE and FE positions and rotating one CH_3NH_3^+ cation stepwise by 180° . The intermediate configurations were not necessarily relaxed to determine the polarization quanta; therefore, static calculations were used here, which is slightly different from the approach used in ref 28.

The PBC-induced ambiguity in the calculated dipole moment was determined using the method described above, and the derived smooth curves of the dipole moments along the three axes are shown in Figure 2b. In the $1 \times 2 \times 1$ FE

supercell of 251.06 \AA^3 , the dipole moment is $(0, 1.10, 4.06) \text{ e\AA}$, and the polarization magnitude is thus calculated to be 13.42 \mu C/cm^2 , in good agreement with the literature.²⁸ The value reported in ref 40 is much larger, at 38 \mu C/cm^2 , which might be due to the neglect of polarization quanta.²⁸ Note here that the polarization of the constructed AFE configuration is not strictly zero, because the CH_3NH_3^+ cations are not necessarily translated inside the inorganic lattice to ensure that the oppositely charged monopoles to coincide.

The polarization has three sources: off-center displacement of Pb within the PbI_6 octahedron, polarization within CH_3NH_3^+ , and off-center displacement of the CH_3NH_3^+ charge center within the inorganic lattice.⁴⁷ By conducting separate calculations for the inorganic lattice (with two units of negative charge) and the organic cation (with two units of positive charge) alone, we identified the individual contributions. Actually, the curves in Figure 2b can be approximately considered as the superimposition of sinusoidal curves and linear curves for the cation rotation and the linearly translated inorganic lattice, respectively. Our calculations show that the off-center displacement of Pb within the PbI_6 octahedron constitutes the major polarization source, namely, $(0, 1.24, 5.61) \text{ \mu C/cm}^2$ or 5.74 \mu C/cm^2 in magnitude, whereas the polarization within CH_3NH_3^+ contributes $(0, 1.43, 4.47) \text{ \mu C/cm}^2$ or 4.70 \mu C/cm^2 in magnitude (see Table 1). The last contribution from the off-center displacement of the CH_3NH_3^+ charge center within the inorganic lattice is therefore identified by subtraction of the two other parts from the total polarization, giving $(0, 0.84, 2.87) \text{ \mu C/cm}^2$ or 2.99 \mu C/cm^2 in magnitude. This indicates a 0.47 \AA distance from the monopole charge centers.

In contrast to the cubic phase, the tetragonal phase has a polarization of 6.8 ,⁴⁰ 8 ,⁴⁷ or 4.42 ²⁸ \mu C/cm^2 , with the CH_3NH_3^+ cations contributing the major portion.⁴⁷ This discrepancy is due to the weaker off-center motion of Pb in the tetragonal phase, which is $\sim 0.07 \text{ \AA}$.⁴⁰ In the equilibrium tetragonal phase, the neighboring C–N bonds get crossed in both the $[001]$ and $[011]$ directions, and the CH_3NH_3^+ dipole significantly tilts out of the base plane (*boc* plane here),⁴⁷ which alleviates the distortion of the PbI_6 octahedron.

CL-DOPED IODIDE

Because the three I ion sites in the $\text{CH}_3\text{NH}_3\text{PbI}_3$ cubic unit cell are nonequivalent, we constructed three Cl-substituted configurations (cases I, II, and III) and relaxed them as shown in Table 1. The polarizations of the three configurations were calculated the same way as above, and the results are listed in Table 1. One can see that, except for a minor decrease in case I, the polarization of the Cl-substituted configuration increased compared to that of the pure iodide. For case III, the polarization exhibited a significant 53% increase. The off-center displacement of Pb within the PbX_6 octahedron still constituted the most significant polarization source and was mainly responsible for the total polarization increase. The relative energy difference increased to 0.11 eV , compared to an upper limit of $\sim 30 \text{ meV}$ caused by different orientation of CH_3NH_3^+ in $\text{CH}_3\text{NH}_3\text{PbI}_3$. This is due to the asymmetry introduced by the partial doping of Cl. At elevated temperatures for the cubic phase, the polarization can be the weighted average of cases I, II, and III because of the disordered orientations of the organic cation.

Even though the electronegativity of the halogen increases upon Cl (3.16) substitution for I (2.66),⁴⁸ the inorganic lattice

is not necessarily more distorted in the Cl-doped iodide, and thus, the inorganic lattice polarization is not necessarily larger (Table 1). It is interesting to examine the different effects of Cl doping at different sites. Through a detailed investigation of the atomic configurations and charge densities of these structures (see Figure 3), we found that the organic cation undergoes little

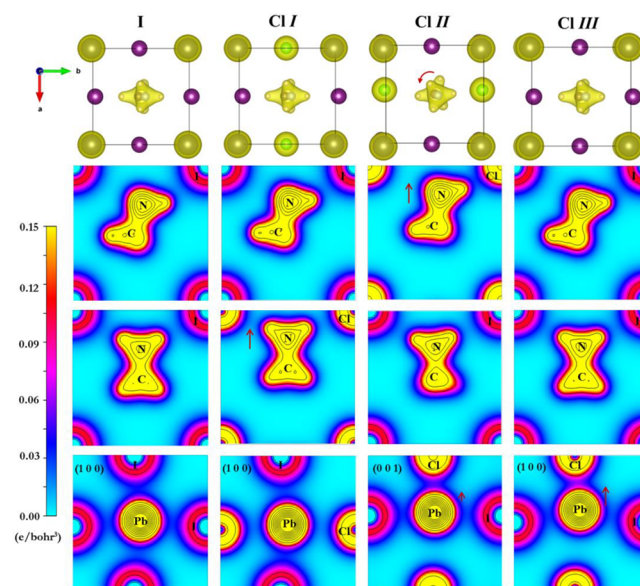


Figure 3. Atomic configurations and charge densities of pure iodide and the three Cl-doped iodides. (Top row) View in the *aob* plane with an isosurface of 0.15 e/bohr^3 charge density. (Middle row) Two-dimensional charge density of the (100) plane intersecting the organic cation. (Bottom row) Two-dimensional charge density of the $\{100\}$ plane showing the interaction between Pb and doped Cl ions. The arrows indicate the relative displacements of ions in Cl-doped iodides compared to pure iodide.

change in direction, except for case II, in which CH_3NH_3^+ is rotated to align more parallel to the $\langle 001 \rangle$ direction ($\sim 8^\circ$ compared to 17.6° in the pure iodide). The total energy of case II is decreased through the stronger hydrogen bond between Cl and N, making case II the configuration with the lowest relative energy among the three configurations. In addition to the cation rotation, the hydrogen bonds also induce more severe octahedral distortion and a stronger ionic bond between the Pb and Cl ions, thus making the polarization along the *a* axis increase. The organic cation drifts closer to the Cl ions on the upper (001) plane in both cases I and II. However, unlike in case II, in case I, the Cl ion is confined at the half-lattice-vector position with little octahedral distortion. In case III, the Cl ion is displaced from the original iodine position, and a stronger Pb–Cl ionic bond forms, which significantly increases the polarization along the *c* axis.

The positions of Cl relative to the organic cation in cases II and III are very similar to the equatorial substitution configuration in the tetragonal phase,^{22,40} because the Pb–X–Pb plane is approximately parallel to the organic cation. In the tetragonal phase, the substitution of Cl (8.3 at. %) at the equatorial site increases the polarization by 22%.⁴⁰ As discussed above for the pure iodide case, the lower symmetry in the tetragonal phase also decreases the magnitude of the polarization for the Cl-doped iodide.

In summary, using first-principles calculations and the Berry phase method, we have investigated the lattice distortion and ferroelectricity of $\text{CH}_3\text{NH}_3\text{PbI}_3$ in the high-temperature cubic phase induced by Cl doping. The off-center displacement of Pb within the PbI_6 octahedron was found to introduce major intrinsic polarization, much more significant than the off-center displacement of CH_3NH_3^+ within the inorganic lattice or charge polarization within the organic cation. Cl-doping-induced lattice distortion could be a general mechanism to further assist charge-carrier separation in solar cell devices as observed in experiments, and similar results can also be expected in Br-doped perovskites.

AUTHOR INFORMATION

Corresponding Author

*E-mail: fluiu@eng.utah.edu.

Notes

The authors declare no competing financial interest.

ACKNOWLEDGMENTS

W.-L.Y. and F.L. acknowledge support by DOE-BES (Grant DEFG02-04ER46148). W.-L.Y. is also thankful for the support from the China Scholarship Council. We thank the CHPC at the University of Utah and DOE-NERSC for providing computing resources.

REFERENCES

- (1) Kojima, A.; Teshima, K.; Shirai, Y.; Miyasaka, T. Organometal Halide Perovskites as Visible-Light Sensitizers for Photovoltaic Cells. *J. Am. Chem. Soc.* **2009**, *131*, 6050–6051.
- (2) Park, N.-G. Organometal Perovskite Light Absorbers Toward a 20% Efficiency Low-Cost Solid-State Mesoscopic Solar Cell. *J. Phys. Chem. Lett.* **2013**, *4*, 2423–2429.
- (3) Snaith, H. J. Perovskites: The Emergence of a New Era for Low-Cost, High-Efficiency Solar Cells. *J. Phys. Chem. Lett.* **2013**, *4*, 3623–3630.
- (4) Im, J.-H.; Lee, C.-R.; Lee, J.-W.; Park, S.-W.; Park, N.-G. 6.5% Efficient Perovskite Quantum-Dot-Sensitized Solar Cell. *Nanoscale* **2011**, *3*, 4088–4093.
- (5) Kim, H.-S.; Lee, C.-R.; Im, J.-H.; Lee, K.-B.; Moehl, T.; Marchioro, A.; Moon, S.-J.; Humphry-Baker, R.; Yum, J.-H.; Moser, J. E.; Grätzel, M.; Park, N.-G. Lead Iodide Perovskite Sensitized All-Solid-State Submicron Thin Film Mesoscopic Solar Cell with Efficiency Exceeding 9%. *Sci. Rep.* **2012**, *2*, 591.
- (6) Lee, M. M.; Teuscher, J.; Miyasaka, T.; Murakami, T. N.; Snaith, H. J. Efficient Hybrid Solar Cells Based on Meso-Superstructured Organometal Halide Perovskites. *Science* **2012**, *338*, 643–647.
- (7) Burschka, J.; Pellet, N.; Moon, S.-J.; Humphry-Baker, R.; Gao, P.; Nazeeruddin, M. K.; Grätzel, M. Sequential Deposition as a Route to High-Performance Perovskite-Sensitized Solar Cells. *Nature* **2013**, *499*, 316–319.
- (8) Liu, M.; Johnston, M. B.; Snaith, H. J. Efficient Planar Heterojunction Perovskite Solar Cells by Vapour Deposition. *Nature* **2013**, *501*, 395–398.
- (9) Zhou, H.; Chen, Q.; Li, G.; Luo, S.; Song, T.-b.; Duan, H.-S.; Hong, Z.; You, J.; Liu, Y.; Yang, Y. Interface Engineering of Highly Efficient Perovskite Solar Cells. *Science* **2014**, *345*, 542–546.
- (10) National Renewable Energy Laboratory. Best Research-Cell Efficiencies. http://www.nrel.gov/ncpv/images/efficiency_chart.jpg (accessed May 26, 2016).
- (11) Poglitsch, A.; Weber, D. Dynamic Disorder in Methylammoniumtrihalogenoplumbates (II) Observed by Millimeter-Wave Spectroscopy. *J. Chem. Phys.* **1987**, *87*, 6373–6378.
- (12) Onoda-Yamamuro, N.; Matsuo, T.; Suga, H. Calorimetric and IR Spectroscopic Studies of Phase Transitions in Methylammonium Trihalogenoplumbates (II). *J. Phys. Chem. Solids* **1990**, *51*, 1383–1395.
- (13) Kawamura, Y.; Mashiyama, H.; Hasebe, K. Structural Study on Cubic–Tetragonal Transition of $\text{CH}_3\text{NH}_3\text{PbI}_3$. *J. Phys. Soc. Jpn.* **2002**, *71*, 1694–1697.
- (14) Baikie, T.; Fang, Y.; Kadro, J. M.; Schreyer, M.; Wei, F.; Mhaisalkar, S. G.; Grätzel, M.; White, T. J. Synthesis and Crystal Chemistry of the Hybrid Perovskite $(\text{CH}_3\text{NH}_3)\text{PbI}_3$ for Solid-State Sensitized Solar Cell Applications. *J. Mater. Chem. A* **2013**, *1*, 5628–5641.
- (15) Stoumpos, C. C.; Malliakas, C. D.; Kanatzidis, M. G. Semiconducting Tin and Lead Iodide Perovskites with Organic Cations: Phase Transitions, High Mobilities, and Near-Infrared Photoluminescent Properties. *Inorg. Chem.* **2013**, *52*, 9019–9038.
- (16) Brivio, F.; Walker, A. B.; Walsh, A. Structural and Electronic Properties of Hybrid Perovskites for High-Efficiency Thin-Film Photovoltaics from First-Principles. *APL Mater.* **2013**, *1*, 042111.
- (17) Giorgi, G.; Fujisawa, J.-I.; Segawa, H.; Yamashita, K. Cation Role in Structural and Electronic Properties of 3D Organic-Inorganic Perovskite Halides: A DFT Analysis. *J. Phys. Chem. C* **2014**, *118*, 12176–12183.
- (18) Motta, C.; El-Mellouhi, F.; Kais, S.; Tabet, N.; Alharbi, F.; Sanvito, S. Revealing the Role of Organic Cations in Hybrid Halide Perovskite $\text{CH}_3\text{NH}_3\text{PbI}_3$. *Nat. Commun.* **2015**, *6*, 7026.
- (19) Frost, J. M.; Butler, K. T.; Brivio, F.; Hendon, C. H.; van Schilfgaarde, M.; Walsh, A. Atomistic Origins of High-Performance in Hybrid Halide Perovskite Solar Cells. *Nano Lett.* **2014**, *14*, 2584–2590.
- (20) Ball, J. M.; Lee, M. M.; Hey, A.; Snaith, H. J. Low-Temperature Processed Meso-Superstructured to Thin-Film Perovskite Solar Cells. *Energy Environ. Sci.* **2013**, *6*, 1739–1743.
- (21) Jiang, M.; Wu, J.; Lan, F.; Tao, Q.; Gao, D.; Li, G. Enhancing the Performance of Planar Organo-Lead Halide Perovskite Solar Cells by Using a Mixed Halide Source. *J. Mater. Chem. A* **2015**, *3*, 963–967.
- (22) Stranks, S. D.; Eperon, G. E.; Grancini, G.; Menelaou, C.; Alcocer, M. J. P.; Leijtens, T.; Herz, L. M.; Petrozza, A.; Snaith, H. J. Electron-Hole Diffusion Lengths Exceeding 1 Micrometer in an Organometal Trihalide Perovskite Absorber. *Science* **2013**, *342*, 341–344.
- (23) Mosconi, E.; Amat, A.; Nazeeruddin, M. K.; Grätzel, M.; De Angelis, F. First-Principles Modeling of Mixed Halide Organometal Perovskites for Photovoltaic Applications. *J. Phys. Chem. C* **2013**, *117*, 13902–13913.
- (24) Colella, S.; Mosconi, E.; Fedeli, P.; Listorti, A.; Gazza, F.; Orlandi, F.; Ferro, P.; Besagni, T.; Rizzo, A.; Calestani, G.; Gigli, G.; De Angelis, F.; Mosca, R. $\text{MAPbI}_{3-x}\text{Cl}_x$ Mixed Halide Perovskite for Hybrid Solar Cells: The Role of Chloride as Dopant on the Transport and Structural Properties. *Chem. Mater.* **2013**, *25*, 4613–4618.
- (25) Yu, H.; Wang, F.; Xie, F.; Li, W.; Chen, J.; Zhao, N. The Role of Chlorine in the Formation Process of $\text{CH}_3\text{NH}_3\text{PbI}_{3-x}\text{Cl}_x$ Perovskite. *Adv. Funct. Mater.* **2014**, *24*, 7102–7108.
- (26) Unger, E. L.; Bowring, A. R.; Tassone, C. J.; Pool, V. L.; Gold-Parker, A.; Checharoen, R.; Stone, K. H.; Hoke, E. T.; Toney, M. F.; McGehee, M. D. Chloride in Lead Chloride-Derived Organo-Metal Halides for Perovskite-Absorber Solar Cells. *Chem. Mater.* **2014**, *26*, 7158–7165.
- (27) Frisch, M. J.; Trucks, G. W.; Schlegel, H. B.; Scuseria, G. E.; Robb, M. A.; Cheeseman, J. R.; Scalmani, G.; Barone, V.; Mennucci, B.; Petersson, G. A.; Nakatsuji, H.; Caricato, M.; Li, X.; Hratchian, H. P.; Izmaylov, A. F.; Bloino, J.; Zheng, G.; Sonnenberg, J. L.; Hada, M.; Ehara, M.; Toyota, K.; Fukuda, R.; Hasegawa, J.; Ishida, M.; Nakajima, T.; Honda, Y.; Kitao, O.; Nakai, H.; Vreven, T.; Montgomery, J. A., Jr.; Peralta, J. E.; Ogliaro, F.; Bearpark, M.; Heyd, J. J.; Brothers, E.; Kudin, K. N.; Staroverov, V. N.; Keith, T.; Kobayashi, R.; Normand, J.; Raghavachari, K.; Rendell, A.; Burant, J. C.; Iyengar, S. S.; Tomasi, J.; Cossi, M.; Rega, N.; Millam, J. M.; Klene, M.; Knox, J. E.; Cross, J. B.; Bakken, V.; Adamo, C.; Jaramillo, J.; Gomperts, R.; Stratmann, R. E.; Yazyev, O.; Austin, A. J.; Cammi, R.; Pomelli, C.; Ochterski, J. W.; Martin, R. L.; Morokuma, K.; Zakrzewski, V. G.; Voth, G. A.; Salvador, P.; Dannenberg, J. J.; Dapprich, S.; Daniels, A. D.; Farkas, O.;

Foresman, J. B.; Ortiz, J. V.; Cioslowski, J.; Fox, D. J. *Gaussian 09*, revision D.01; Gaussian, Inc.: Wallingford, CT, 2013.

(28) Stroppa, A.; Quarti, C.; De Angelis, F.; Picozzi, S. Ferroelectric Polarization of $\text{CH}_3\text{NH}_3\text{PbI}_3$: A Detailed Study Based on Density Functional Theory and Symmetry Mode Analysis. *J. Phys. Chem. Lett.* **2015**, *6*, 2223–2231.

(29) Kresse, G.; Furthmüller, J. Efficient Iterative Schemes for *ab Initio* Total-Energy Calculations Using a Plane-Wave Basis Set. *Phys. Rev. B: Condens. Matter Mater. Phys.* **1996**, *54*, 11169–11186.

(30) Blöchl, P. E. Projector Augmented-Wave Method. *Phys. Rev. B: Condens. Matter Mater. Phys.* **1994**, *50*, 17953–17979.

(31) Kresse, G.; Joubert, D. From Ultrasoft Pseudopotentials to the Projector Augmented-Wave Method. *Phys. Rev. B: Condens. Matter Mater. Phys.* **1999**, *59*, 1758–1775.

(32) Perdew, J. P.; Ruzsinszky, A.; Csonka, G. I.; Vydrov, O. A.; Scuseria, G. E.; Constantin, L. A.; Zhou, X.; Burke, K. Restoring the Density-Gradient Expansion for Exchange in Solids and Surfaces. *Phys. Rev. Lett.* **2008**, *100*, 136406.

(33) Perdew, J. P.; Burke, K.; Ernzerhof, M. Generalized Gradient Approximation Made Simple. *Phys. Rev. Lett.* **1996**, *77*, 3865–3868.

(34) Blöchl, P. E.; Jepsen, O.; Andersen, O. K. Improved Tetrahedron Method for Brillouin-Zone Integrations. *Phys. Rev. B: Condens. Matter Mater. Phys.* **1994**, *49*, 16223–16233.

(35) Monkhorst, H. J.; Pack, J. D. Special Points for Brillouin-Zone Integrations. *Phys. Rev. B* **1976**, *13*, 5188–5192.

(36) Brivio, F.; Butler, K. T.; Walsh, A.; van Schilfgaarde, M. Relativistic Quasiparticle Self-Consistent Electronic Structure of Hybrid Halide Perovskite Photovoltaic Absorbers. *Phys. Rev. B: Condens. Matter Mater. Phys.* **2014**, *89*, 155204.

(37) Umari, P.; Mosconi, E.; De Angelis, F. Relativistic GW Calculations on $\text{CH}_3\text{NH}_3\text{PbI}_3$ and $\text{CH}_3\text{NH}_3\text{SnI}_3$ Perovskites for Solar Cell Applications. *Sci. Rep.* **2014**, *4*, 4467.

(38) Even, J.; Pedesseau, L.; Jancu, J.-M.; Katan, C. Importance of Spin–Orbit Coupling in Hybrid Organic/Inorganic Perovskites for Photovoltaic Applications. *J. Phys. Chem. Lett.* **2013**, *4*, 2999–3005.

(39) Amat, A.; Mosconi, E.; Ronca, E.; Quarti, C.; Umari, P.; Nazeeruddin, Md. K.; Grätzel, M.; De Angelis, F. Cation-Induced Band-Gap Tuning in Organohalide Perovskites: Interplay of Spin-Orbit Coupling and Octahedra Tilting. *Nano Lett.* **2014**, *14*, 3608–3616.

(40) Zheng, F.; Takenaka, H.; Wang, F.; Koocher, N. Z.; Rappe, A. M. First-Principles Calculation of the Bulk Photovoltaic Effect in $\text{CH}_3\text{NH}_3\text{PbI}_3$ and $\text{CH}_3\text{NH}_3\text{PbI}_{3-x}\text{Cl}_x$. *J. Phys. Chem. Lett.* **2015**, *6*, 31–37.

(41) Birch, F. Finite Elastic Strain of Cubic Crystals. *Phys. Rev.* **1947**, *71*, 809–824.

(42) Momma, K.; Izumi, F. VESTA 3 for Three-Dimensional Visualization of Crystal, Volumetric and Morphology Data. *J. Appl. Crystallogr.* **2011**, *44*, 1272–1276.

(43) King-Smith, R. D.; Vanderbilt, D. Theory of Polarization of Crystalline Solids. *Phys. Rev. B: Condens. Matter Mater. Phys.* **1993**, *47*, 1651–1654.

(44) Vanderbilt, D.; King-Smith, R. D. Electric Polarization as a Bulk Quantity and Its Relation to Surface Charge. *Phys. Rev. B: Condens. Matter Mater. Phys.* **1993**, *48*, 4442–4455.

(45) Resta, R. Macroscopic Polarization in Crystalline Dielectrics: The Geometric Phase Approach. *Rev. Mod. Phys.* **1994**, *66*, 899–915.

(46) Neaton, J. B.; Ederer, C.; Waghmare, U. V.; Spaldin, N. A.; Rabe, K. M. First-Principles Study of Spontaneous Polarization in Multiferroic BiFeO_3 . *Phys. Rev. B: Condens. Matter Mater. Phys.* **2005**, *71*, 014113.

(47) Fan, Z.; Xiao, J.; Sun, K.; Chen, L.; Hu, Y.; Ouyang, J.; Ong, K. P.; Zeng, K.; Wang, J. Ferroelectricity of $\text{CH}_3\text{NH}_3\text{PbI}_3$ Perovskite. *J. Phys. Chem. Lett.* **2015**, *6*, 1155–1161.

(48) Pauling, L. *The Nature of the Chemical Bond*, 3rd ed.; Cornell University: Ithaca, NY, 1960.